Supporting information

Thermal Energy Transport across the Interface between Phase Change Material *n*-Heneicosane in Solid and Liquid Phases and Few-Layer Graphene

Hari Krishna Chilukoti[1,a,], Tianhang Zhou[1,a], Vikram Reddy Ardham[2], Michael C. Böhm[1] and Florian Müller-Plathe[1]*

[1] Technische Universität Darmstadt, Eduard-Zintl-Institut für Anorganische und Physikalische Chemie, 64287 Darmstadt, Germany.

[2] Department of Biology, University of Fribourg, Chemin du Musée 10, 1700 Fribourg, Switzerland.

Force field parameters

Table S1. The NERD potential parameters for *n*-heneicosane[24].

	Potential form	Parameters
Bond stretching potential	$\frac{V(r)}{k_B} = \frac{k_r}{2}\left(r - b_{eq}\right)^2$	k_r = 96500 K/Å^2 b_{eq} = 1.54 Å
Bond bending potential	$\frac{V(\theta)}{k_B} = \frac{k_\theta}{2}\left(\theta - \theta_{eq}\right)^2$	k_θ = 62500 K/rad^2 θ_{eq} = 114.0°
Torsion potential	$\frac{V(\phi)}{k_B} = V_0 + V_1\left(1+\cos\phi\right) + V_2\left(1-\cos 2\phi\right) + V_3\left(1+\cos 3\phi\right)$	V_0 = 0 K, V_1 = 355.04 K, V_2 = -68.19 K, V_3 = 701.32 K

Table S2. Optimized Tersoff potential parameters for graphene[25]

A = 1393.6 eV	B = 430.0 eV
λ_1 = 3.4879 Å^{-1}	λ_2 = 2.2119 Å^{-1}
λ_3 = 0.0000 Å^{-1}	n = 0.72751
c = 38049.0	β = 1.5724×10^{-7}
d = 4.3484	h = -0.930
R = 1.95 Å	D = 0.15 Å

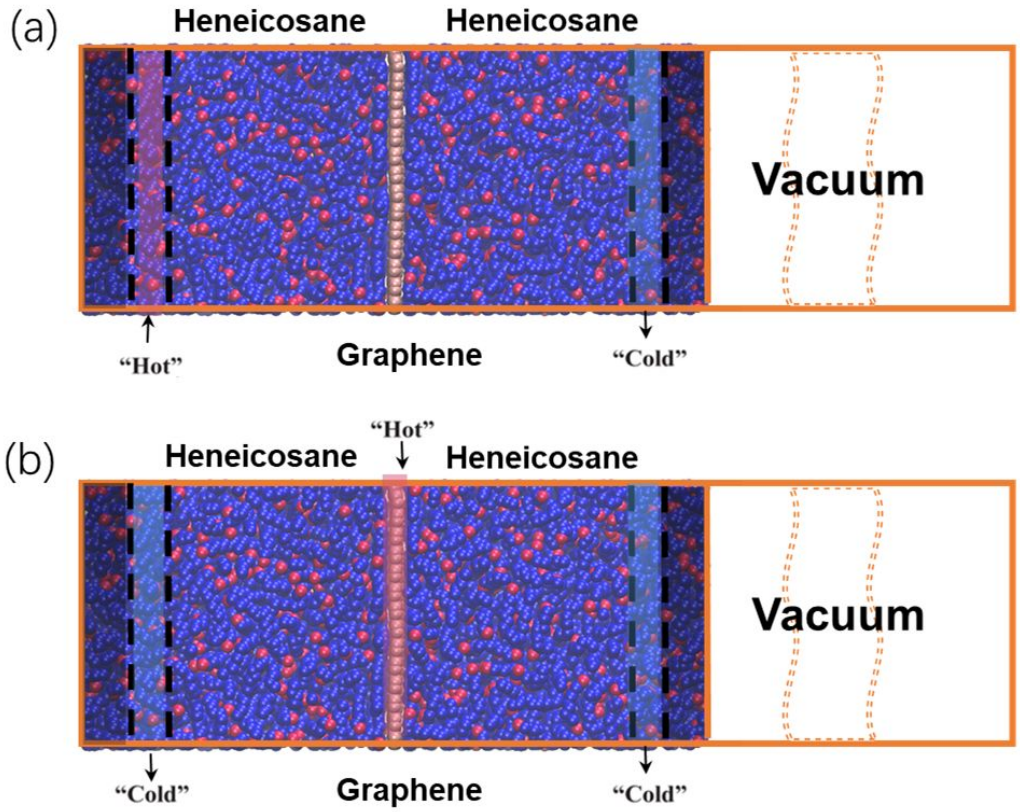

Figure S1. Snapshots of a monolayer graphene-liquid heneicosane system under (a) heat-matrix mode and (b) heat-graphene mode. Heat source and heat sink region are labeled as "hot" and “cold”, respectively. The non-equlibrium molecular dynmaics simulations have been performed for both modes.

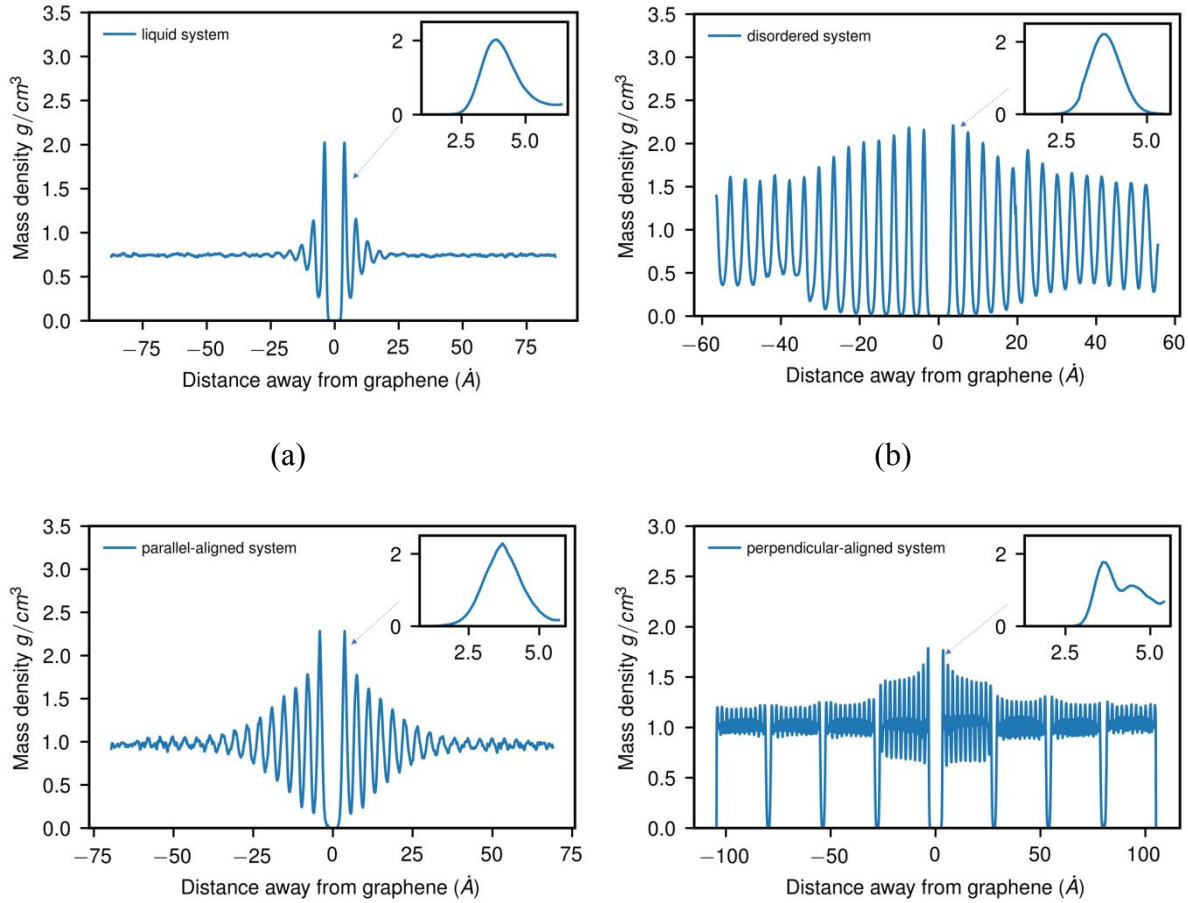

Figure S2. Density distributions in heneicosane along the *z*-axis in (a) liquid heneicosane-monolayer graphene system at 400 K and 1 atm (b) disordered heneicosane-monolayer graphene system at 250 K and 1 atm. One of the three systems constructed is shown here (c) parallel aligned heneicosane-monolayer graphene system at 250 K and 1 atm. (d) perpendicular aligned heneicosane-monolayer graphene system at 250 K and 1 atm. The first adsorption layer is shown an inset of each figure. The density profiles are plotted with respect to the position of graphene. The zero on *x*-axis represent the position of graphene.

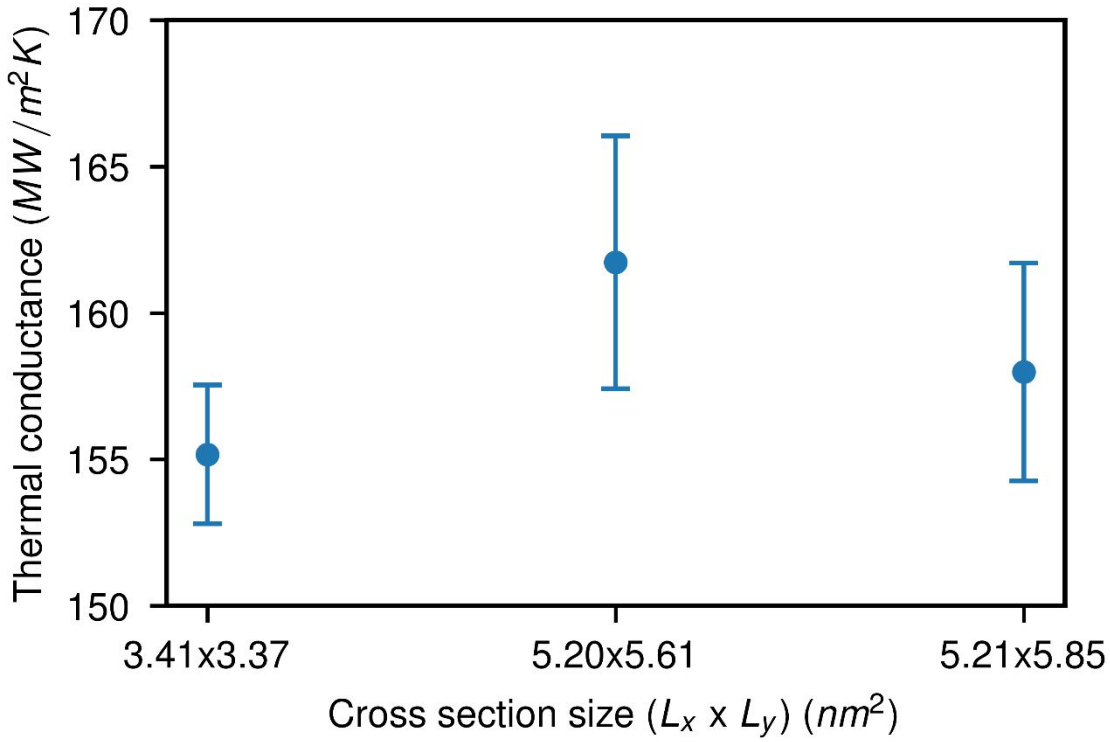

Figure S3. Variation of the interfacial thermal conductance at the interface between liquid heneicosane and monolayer graphene as a function of cross section size of the computational system under the heat-matrix mode at 350 K and 1 atm. The error bars have been symbolized by vertical lines.

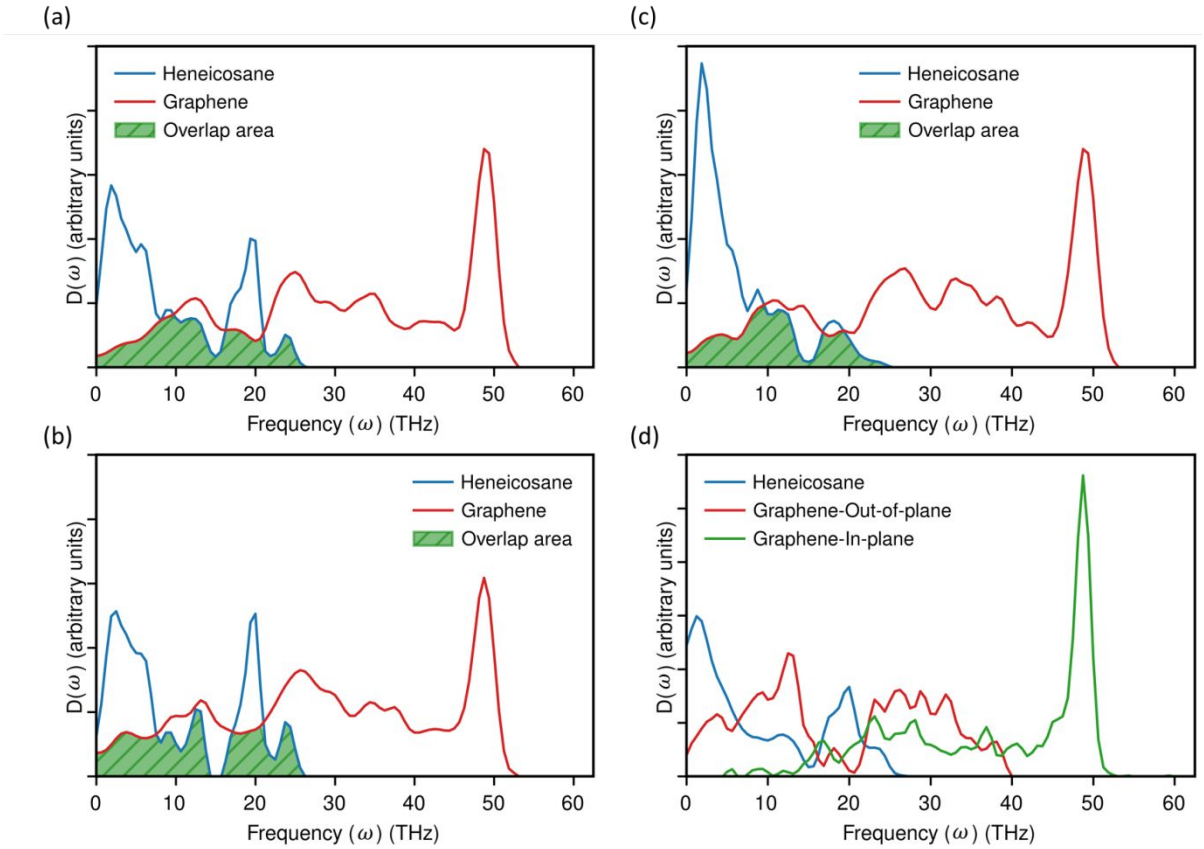

Figure S4. Overall vibrational density of states (VDOS), $D(\omega)$, of a monolayer graphene and heneicosane in arbitary units for the interface between: (a) graphene and amorphous heneicosane at 250 K and 1 atm, (b) graphene and parallel-aligned heneicosane crystal at 250 K and 1 atm, (c) graphene and perpendicualr-aligend heneicosane crystal at 250 K and 1 atm. (d) The VDOS profiles in arbitary units of a monolayer graphene-liquid heneicosane system at 350 K and 1 atm; the in-plane and out-of-plane VDOS of graphene is shown in the figure.

Pressure in simulation systems

Note that the local pressure at the interface is different in the normal and lateral directions due to the interfacial tension. As an example, we have calculated pressure components along normal (z) and lateral directions (x and y) distributions along the z-direction in a monolayer graphene-liquid heneicosane system under NPT ensemble at 400 K and 1 atm as shown in Fig. S5. For the calculation of pressure, the data were collected for 4 ns. It is noticed that the pressure components in the bulk liquid region are same in all three directions and are extremely close to the target pressure (Fig. S5). Fujiwara and Shibahara[S1] have shown that the normal pressure component to the interface should be constant throughout the liquid in the solid-liquid interface region at mechanical equilibrium. However, it should be noted that the procedure adopted by Fujiwara and Shibahara[S1] for the pressure calculation is an approximated one. We notice that the normal pressure component fluctuates in the interface regions, which is primarily attributed to the algorithm used in the LAMMPS for calculating pressure.[S2] The algorithm in LAMMPS neglects higher order terms of the Irving and Kirkwood method.[S3-S4] Varnik et al.[S3] showed that pressure oscillations in the interface region depends on the expressions retained in the calculation of pressure tensor. They concluded that the oscillations on the normal pressure are not unphysical and the important points are recovery of normal pressure in the bulk region and correct value of the surface tension. Similar types of fluctuations have been reported in the past studies[S5-S7], where the LAMMPS had been used for simulations.

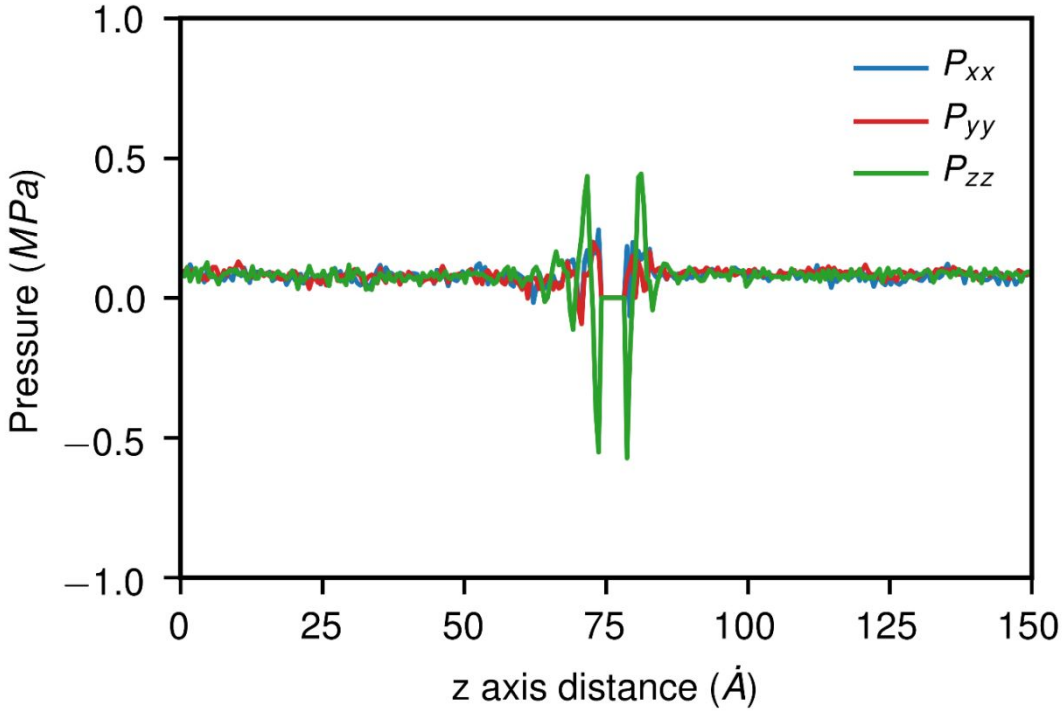

Figure S5. Liquid heneicosane pressure components P_{xx}(z), P_{yy}(z), P_{zz}(z) distribution in the direction normal to the interface for the liquid heneicosane-monolayer graphene at 400 K and 1 atm

Spectral heat flux and VDOS

It should be noted that the output forces and velocities has three components along Cartesian coordinates. The components along *x*- and *y*-axis describe transverse or in-plane mode contributions to total VDOS and total spectral heat flux. The in-plane VDOS and in-plane spectral heat flux are calculated as follows

$$D(\omega)_{\text{in-plane}} = \frac{1}{k_B T}\sum_i m_i \int_{-\infty}^{+\infty} d\tau e^{i\omega\tau} \left\langle v_{xy,i}(\tau)\cdot v_{xy,i}(0)\right\rangle \quad \text{(S1)}$$

$$q(\omega)_{\text{in-plane}} = \frac{2}{A}\mathrm{i}\ \sum_{j\in h, i\in g} \int_{-\infty}^{+\infty} d\tau e^{i\omega\tau} \left\langle F_{xy,ij}(\tau)\cdot v_{xy,i}(0)\right\rangle \quad \text{(S2)}$$

Similarly, the components along z-axis describe longitudinal or out-of-plane mode

contributions to total VDOS and total spectral heat flux. The out-of-plane VDOS and out-of-plane spectral heat flux are calculated as follows

$$D(\omega)_{\text{out-of-plane}} = \frac{1}{k_B T} \sum_i m_i \int_{-\infty}^{+\infty} d\tau e^{i\omega\tau} \left\langle v_{z,i}(\tau) \cdot v_{z,i}(0) \right\rangle \tag{S3}$$

$$q(\omega)_{\text{out-of-plane}} = \frac{2}{A} \mathrm{i} \sum_{j \in h, i \in g} \int_{-\infty}^{+\infty} d\tau e^{i\omega\tau} \left\langle F_{z,ij}(\tau) \cdot v_{z,i}(0) \right\rangle \tag{S4}$$

As expected, the summation of in-plane and out-of-plane spectrally resolved heat flux gives the total spectral heat flux. $q(\omega)_{\text{total}} = q(\omega)_{\text{in-plane}} + q(\omega)_{\text{out-of-plane}}$. Normalized cumulative heat flux is calculated as follows

$$\text{Normalized cumulative } q_i(\omega) = \int_0^{\infty} \frac{q_i(\omega)}{\int_0^{\infty} q_{\text{total}}(\omega)} d\omega \tag{S5}$$

where i = in-plane, out-of-plane, total

Width of heating region influence on thermal conductance

To investigate the effect of the width of control regions, we have performed a few additional simulations with larger heating regions. We have injected heat into all graphene layers in a three-layer graphene system, fiver-layer graphene system and seven-layer graphene system. The width of heating regions is different in all three systems. The simulations performed in this manner correspond to the single-layer graphene system under heat-graphene mode. Additionally, we have also heated the central three layers in a seven-layer graphene system (shown in Fig. S6). It is observed that the interfacial thermal conductance values are close to the same within the error bars irrespective of the widths of the controlling regions. Therefore, we conclude that the width of the controlling region does not have significant influence on the results obtained in this study.

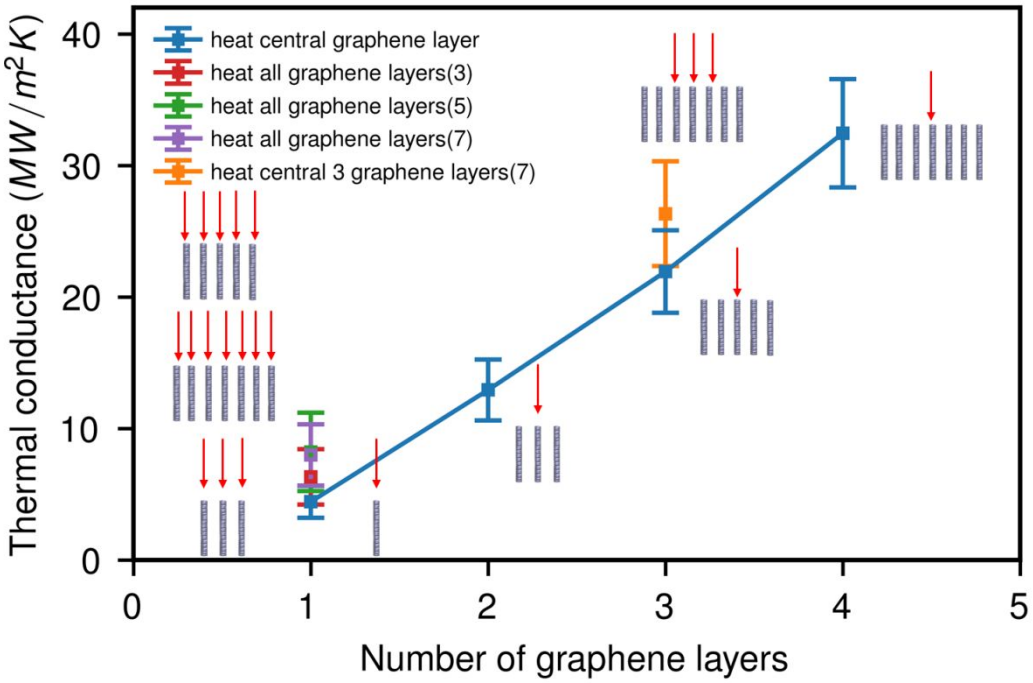

Figure S6. Interfacial thermal conductance between liquid heneicosane and graphene with different widths of heating regions at 400 K and 1 atm.

References

S1. Fujiwara, K.; Shibahara, M., Local Pressure Components and Interfacial Tension at a Liquid-Solid Interface Obtained by the Perturbative Method in the Lennard-Jones System. *J Chem Phys* **2014**, *141*, 034707.

S2. Bekker, H.; Dijkstra, E. J.; Renardus, M. K. R.; Berendsen, H. J. C., An Efficient, Box Shape Independent Non-Bonded Force and Virial Algorithm for Molecular Dynamics. *Molecular Simulation* **1995**, *14*, 137-151.

S3. Varnik, F.; Baschnagel, J.; Binder, K., Molecular Dynamics Results on the Pressure Tensor of Polymer Films. *The Journal of Chemical Physics* **2000**, *113*, 4444-4453.

S4. Todd, B. D.; Evans, D. J.; Daivis, P. J., Pressure Tensor for Inhomogeneous Fluids. *Phys Rev E Stat Phys Plasmas Fluids Relat Interdiscip Topics* **1995**, *52*, 1627-1638.

S5. Pham, A.; Barisik, M.; Kim, B., Pressure Dependence of Kapitza Resistance at Gold/Water and Silicon/Water Interfaces. *J Chem Phys* **2013**, *139*, 244702.

S6. Mendonca, A. C.; Padua, A. A.; Malfreyt, P., Nonequilibrium Molecular Simulations of New Ionic Lubricants at Metallic Surfaces: Prediction of the Friction. *J Chem Theory Comput* **2013**, *9*, 1600-10.

S7 Yamaguchi, Y.; Kusudo, H.; Surblys, D.; Omori, T.; Kikugawa, G., Interpretation of Young's equation for a liquiddroplet on a flat and smooth solid surface:Mechanical and thermodynamic routeswith a simple Lennard-Jones liquid. *J Chem Phys* **2019**, *140*, 044701.